STRUCTURAL SCIENCE
CRYSTAL ENGINEERING
MATERIALS

ISSN: 2052-5206
journals.iucr.org/b

Anomalous X-ray diffraction study of Pr-substituted $BaCeO_{3-\delta}$

Juan F. Basbus, Alberto Caneiro, Leopoldo Suescun, Diego G. Lamas and Liliana V. Mogni

Acta Cryst. (2015). B**71**, 455–462

STRUCTURAL SCIENCE CRYSTAL ENGINEERING MATERIALS

ISSN 2052-5206

Anomalous X-ray diffraction study of Pr-substituted $BaCeO_{3-\delta}$

Juan F. Basbus,[a] Alberto Caneiro,[a] Leopoldo Suescun,[b] Diego G. Lamas[c] and Liliana V. Mogni[a]*

[a]CONICET–CNEA, Centro Atómico Bariloche, Av. Bustillo 9500, (8400) S. C. de Bariloche, Rio Negro, Argentina, [b]Cryssmat-Lab/DETEMA, Facultad de Química, Universidad de la República, Montevideo, Uruguay, and [c]CONICET, Escuela de Ciencia y Tecnología, Universidad Nacional de Gral. San Martín, Martín de Irigoyen 3100, (1650) San Martín, Provincia de Buenos Aires, Argentina. *Correspondence e-mail: mogni@cab.cnea.gov.ar

Received 30 December 2014
Accepted 27 May 2015

Edited by D. G. Billing, University of the Witwatersrand, South Africa

Keywords: anomalous X-ray diffraction; synchrotron X-ray diffraction; electronic and ionic mobility; proton conductor; solid oxide fuel cells.

Supporting information: this article has supporting information at journals.iucr.org/b

The effect of Pr doping on the crystal structure and site occupancy was studied for the nominally synthesized $BaCe_{1-x}Pr_xO_{3-\delta}$ (x = 0, 0.2, 0.4, 0.6 and 0.8) perovskites using anomalous X-ray powder diffraction (AXRD) data and Rietveld analysis. Crystal structure parameters were accurately determined using 10 000 eV photons, and the Pr occupancy was refined using data collected with 5962 eV photons, close to the Pr L_{III} absorption edge. $BaCe_{1-x}Pr_xO_{3-\delta}$ crystallizes in the *Pnma* (No. 62) space group for all x values. Pr cations are mainly located at the Ce sites (perovskites B site), but a small fraction of them increasingly substitute some of the Ba ions at the A site as Pr content increases. The Pr doping introduces electronic defects (Pr^{+3}/Pr^{+4}) and oxygen vacancies needed for H_2O incorporation and H-ionic conductivity. A decrease in the orthorhombic distortion would produce the opposite effects on the electronic and ionic mobility. The electronic mobility should increase due to an improvement in the overlap of the (Ce/Pr)4*f*–O2*p* orbital, while the proton mobility should decrease as a consequence of a larger hopping distance.

1. Introduction

Solid oxide fuel cells based on proton-conducting oxides (PC-SOFC) are electrochemical devices that transform chemical energy from hydrogen into electricity with high efficiency, low environmental impact, moderate operating temperatures, good stability and durability (Iwahara *et al.*, 1990; Norby, 1999; Zuo *et al.*, 2006). Previous research indicates that doped barium cerates are promising electrolytes for PC-SOFC (Iwahara *et al.*, 1988; Medvedev *et al.*, 2014; Liu & Nowick, 1992; Pelletier *et al.*, 2005), since the partial substitution of cerium by rare earth and/or transition metal trivalent oxides induces oxygen vacancy formation according to

$$2Ce_{Ce}^{x} + Ln_2O_3 + O_O^{x} \rightleftharpoons V_O^{\bullet\bullet} + 2Ln_{Ce}^{\prime} + 2CeO_2. \quad (1)$$

Under the presence of water vapor, the oxygen vacancies are filled with OH^- anions and the conductivity is promoted by the hopping of the interstitial proton through oxygen sites (Glockner *et al.*, 1999; Bonanos, 2001).

$$V_O^{\bullet\bullet} + H_2O + O_O^{x} \rightleftharpoons +2OH_O^{\bullet} \quad (2)$$

The requirements for a good proton conducting electrolyte under operation conditions (673–873 K) involve a low activation energy (Bi *et al.*, 2009) and high protonic concentration at moderate temperatures (Kreuer, 2003; Iwahara *et al.*, 1988).

Some cation substitutions can also promote electronic conductivity in $BaCeO_3$. The highest electrical conductivities among barium cerates are observed in compounds doped by lanthanides (Giannici *et al.*, 2010), such as Gd (Amsif *et al.*,

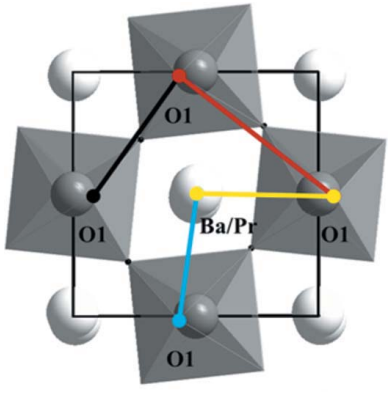

Table 1
Scattering factors expressed in electrons (e^-) for Ba, Ce and Pr atoms at the selected energies.

		10 000 eV		5962 eV	
Atoms	f_0	f'	f''	f'	f''
Ba	56	−0.07	5.50	−8.17	11.67
Ce	58	−0.35	6.80	−10.41	9.88
Pr	59	−0.50	7.30	−20.21	3.75

2011; Kikuchi *et al.*, 2008). Recently, it has been reported that Pr doping improves electrical conductivity, mechanical properties and sintering of these perovskites (Basbus *et al.*, 2014; Magrasó *et al.*, 2011, 2012; Gill *et al.*, 2013; Sharova *et al.*, 2005; Wang & Qiu, 2008). Due to the mixed protonic and electronic conductivities of Pr-doped barium cerates, these materials have also been proposed as potential cathodes (Mukundan *et al.*, 2001) for PC-SOFCs. However, the question regarding the true crystallographic location of lanthanide ions in the $BaCeO_3$ oxides has not been completely answered yet. The two sites of cations in $BaCeO_3$ perovskites exhibit different coordination numbers, 12-fold coordination for *A*-site and sixfold coordination for *B*-site where Ba^{2+}(XII) (ionic radii 1.61 Å) and Ce^{4+}(VI) (ionic radii 0.87 Å) reside, respectively. Some lanthanides could adopt a 12-fold coordination (*i.e.* $r^{XII}_{La^{3+}}$ = 1.36 Å, $r^{XII}_{Pr^{3+}}$ = 1.32 Å, $r^{XII}_{Nd^{3+}}$ = 1.27 Å, $r^{XII}_{Sm^{3+}}$ = 1.24 Å) replacing Ba^{2+} ions and producing $Ln^{\bullet}_{Ba}$ point defects, or a sixfold coordination (*i.e.* $r^{VI}_{La^{3+}}$ = 1.032 Å, $r^{VI}_{Pr^{3+}}$ = 0.99 Å, $r^{VI}_{Nd^{3+}}$ = 0.98 Å, $r^{VI}_{Sm^{3+}}$ = 0.96 Å, $r^{VI}_{Gd^{3+}}$ = 0.938 Å, $r_{Pr^{4+}}VI$ = 0.85 Å) giving place to the Ln'_{Ce} defects. In particular, Pr could enter in both *A* and *B* sites. Extended X-ray absorption fine structure spectroscopy (EXAFS) has already proved to be a useful technique to determine the location of lanthanides in some zirconium and cerium perovskites, where the partial substitution of Zr and Ba by lanthanides decreases the oxygen vacancies, and affects the transport properties (Giannici *et al.*, 2011).

Otherwise, anomalous X-ray diffraction (AXRD) or resonant scattering is also a valuable technique that could be used to differentiate the atomic occupancy in these perovskites (http://skuld.bmsc.washington.edu/scatter/; Hodeau *et al.*, 2001; Cullity & Stock, 1978; Caticha-Ellis, 1981; Welzmiller *et al.*, 2013). This technique is based on the difference in scattering factor of an atom at a wavelength close to an absorption edge of the atom. The atomic scattering factor (f_n) depends on the normal (f_0), real (f') and imaginary (f'') scattering factors as follows

$$f_n = f_0(Q) + f'(\lambda) + if''(\lambda). \quad (3)$$

The real and imaginary parts, known as anomalous dispersion (or resonant scattering) corrections, represent the effect of the ionization and the photon re-emission processes, on the total atomic scattering factor, respectively.

Also, f' is proportional to the wavelength (λ) and the atomic absorption coefficient (μ), and it can be determined experimentally by XAS while f' can be calculated from f' since both anomalous scattering factors are related by the Kramer–Kroning dispersion relation (http://skuld.bmsc.washington.edu/scatter; Hodeau *et al.*, 2001; Palancher *et al.*, 2012). Thus, increasing the energy of the X-ray beam passing through the Pr absorption edge, the real scattering factor f' of Pr decreases by 20 electrons, whereas the imaginary part f'' increases by 4 electrons, whereas the contribution to anomalous scattering by Ba and Ce are smaller than that of Pr, since their L_{III} absorption edges are far from the Pr edge. The goal of this study is to use the contrast produced by the anomalous scattering parameters to determine the structural features of our samples. Table 1 summarizes the scattering factors at 10 000 and 5962 eV for Ba, Ce and Pr (http://skuld.bmsc.washington.edu/scatter/). Despite the atomic scattering factor also being affected by the oxidation state, this effect was not taken into account in the Rietveld analysis of powder diffraction data.

Synchrotron-based anomalous X-ray diffraction (AXRD) have already been used to study the elemental distribution of neighbor atoms between phases in multiphase nanoparticles (Connor *et al.*, 2013), the atomic segregation during the alloying process on binary or ternary alloy films (Yang *et al.*, 2010, 2013) and occupancy factors in specific crystallographic sites for metal oxides spinels and inverse spinels (Perkins *et al.*, 2011; Paudel *et al.*, 2011).

In this work the crystallographic effect of Pr in nominally prepared $BaCe_{1-x}Pr_xO_{3-\delta}$($x$ = 0, 0.2, 0.4, 0.6 and 0.8) perovskites was explored by using synchrotron radiation from the LNLS (Campinas, Brazil) source, at 10 000 and 5962 eV. The effect of Pr doping on the crystallographic parameters such as lattice parameter, atomic position and site occupancy was analyzed.

2. Experimental

Powders with composition $BaCe_{1-x}Pr_xO_{3-\delta}$ (x = 0, 0.2, 0.4, 0.6 and 0.8) were obtained through a modified Pechini method (Basbus *et al.*, 2014) and the phase purity was evaluated by conventional XRD using a PANalytical Empyrean diffractometer. Prior to the XRD study all samples were dehydrated at 1073 K under dry N_2 flow. The structural data were obtained by using X-ray synchrotron radiation from the XPD-D10B beamline at the LNLS, Campinas, Brazil. The experimental configuration includes a Huber diffractometer and Mythen 1 K linear position-sensitive detector. All measurements were performed at room temperature in air, and data were collected by SPEC software. The wavelengths were calibrated using silicon powder from NIST (SRM 640d).

Crystallographic information such as lattice parameters, atomic positions and displacement parameters were obtained by X-ray powder diffraction (XRD) at 10 000 eV, far from the absorption edge of all atoms in the sample. In all cases, the structural models and Wyckoff positions were taken from those reported for $BaCeO_3$ and $BaCe_{0.85}Pr_{0.15}O_3$ by Knight (Knight & Bonanos, 1995) belonging to the space group *Pnma* (Knight, 2001). This information was used as a starting point for the multipattern fit described below. Fig. 1 shows the XRD patterns for all compositions at this energy. The Pr occupancy at the perovskite was evaluated by using anomalous XRD

(AXRD) near to the Pr L_{III} absorption edge, at 5962 eV. The energy for AXRD was selected after performing an energy scan between 5960 and 5980 eV with a step of 0.8 eV at the same beamline as for $BaCe_{0.2}Pr_{0.8}O_{3-\delta}$ sample. In this range the energy resolution of the beamline with the configuration described above is better than 1 eV (Ferreira *et al.*, 2006). Fig. 2 shows the energy scan and its derivate. Note that the L_{III} energy edge of Pr could superimpose with oscillations of L_I and L_{II} edges of Ba ($L_I \simeq 5989$ eV and $L_{II} \simeq 5624$ eV), and L_{III} of Ce ($L_{III} \simeq 5723$ eV).

The normal (10 000 eV) and anomalous (5962 eV) diffraction patterns for each sample were fitted by the Rietveld method by using the multipattern fit mode of the *FullProf* Suite (http://www.ill.eu/sites/fullprof/) with a common structural model (Knight, 2001). A Thompson–Cox–Hastings pseudo-Voigt convoluted with axial divergence asymmetry function was used to fit the peak shape (Finger *et al.*, 1994). The background was refined with a linear interpolation of N selected points. The structural model includes the corrected scattering factor values for anomalous dispersion at the two energies (Table 1), anisotropic atomic displacement parameters for Ba, Ce and Pr atoms, and isotropic atomic displacement for O. The O occupancy was not considered as a refinement variable due to the lower atomic scattering factor of oxygen compared with the heavy ions also present in the sample. However, the O positions and atomic displacement parameters were refined since the tilt of the octahedra is directly related to the structural distortion and the crystal symmetry. The Ba and Ce site occupancies were adjusted or fitted according to the defect model described below by using Kröger–Vink notation; $Pr_{Ba}^{\bullet}$ is Pr^{+3} at the Ba site otherwise, Pr_{Ce}' and Pr_{Ce}^{x} are Pr^{+3} and Pr^{+4} at the Ce sites, respectively. Also, Ce_{Ce}^{x} and V_{Ce}'''' are full and vacant Ce sites and O_O^x and $V_O^{\bullet\bullet}$ correspond to the occupied and vacant oxygen sites, respectively. The $V_O^{\bullet\bullet}$ guarantees the electroneutrality balance, however, as it was explained before, the XRD patterns were fitted considering $[V_O^{\bullet\bullet}] = \delta \simeq 0$. The complete chemical formulae, indicating the different occupation sites (see *Appendix A*), are derived for each model:

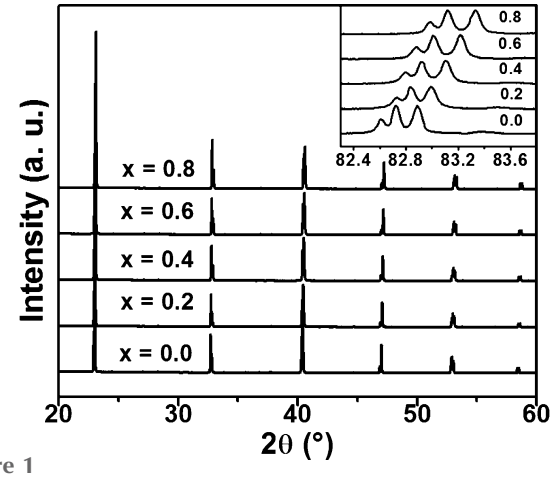

Figure 1
Powder diffraction patterns of $BaCe_{1-x}Pr_xO_{3-\delta}$ (x = 0, 0.2, 0.4, 0.6 and 0.8) at 10 000 eV.

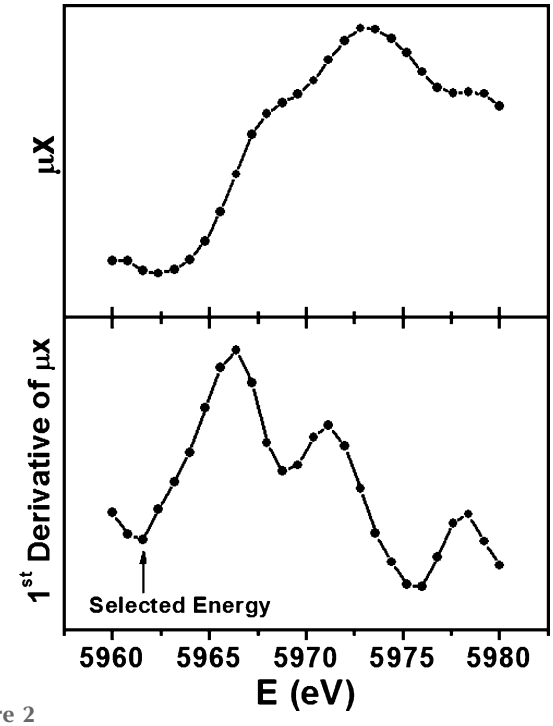

Figure 2
Energy scan and its first derivative, collected close to the Pr L_{III} absorption edge for the higher Pr content ($BaCe_{0.2}Pr_{0.8}O_{3-\delta}$)

Model I: Pr fully located at a Ba site, which means $\sum Pr_{species} = Pr_{Ba}^{\bullet} = x$.

In this model two scenarios are possible:

(i) either Model I is equal to Model III (see below) with $\alpha = x$, where each $Pr_{Ba}^{\bullet} = x$ produces $2x$ Ce-site vacancies and $7x/[2(1+x)]$ oxygen vacancies, that represent as an example 0.33 Ce vacancies and 0.58 oxygen for x = 0.2 (and larger values for larger x); or

(ii) the number of Ce vacancies is the minimum that allows O vacancies to stay close to 0 and x Pr on the Ba site.

The first option represents an unrealistic situation since the required amount of vacant sites at the B and anion sites would preclude the formation of a perovskite structure (such an amount of vacancies are possible at the A site but not at the B site), while the second would imply that the Ba/Ce and Pr/Ce ratios would be lower than the stoichiometric ratio of the nominal composition, therefore a second phase containing Ba and Pr should be present in the sample. However, no secondary phases were detected within the detection limit of the refinement with the data available. Then, Model I was investigated using the following compositional model

$$Ba_{\frac{1}{1+x}}Pr_{\frac{x}{1+x}}Ce_{\frac{1-x}{1-x+y}}V''''_{Ce_{\frac{y}{1-x+y}}}O_{3-\delta}, \qquad \text{(Model I)}$$

where 'y' denotes the minimum amounts of V_{Ce}'''' needed to balance the charge produced as a consequence of Pr^{3+} is located at the A perovskite site, being $y \simeq [x(1-x)]/(4+3x)$.

Model II: Pr fully located at the Ce site, considering $\sum Pr_{species} = Pr_{Ce}' + Pr_{Ce}^{x} = x$

Table 2
Goodness-of-fits from XRD multipattern fits, according to the models for $x = 0.6$.

	10 000 eV			5962 eV		
Model	R_p	R_{wp}	χ^2	R_p	R_{wp}	χ^2
I	8.38	8.01	3.78	13.00	9.59	21.50
II	7.68	6.88	2.79	10.50	6.32	9.37
III	7.75	6.92	2.83	10.40	6.16	8.90

$$BaCe_{1-x}Pr_xO_{3-\delta}, \qquad \text{(Model II)}$$

Model III: Pr-free distributed between Ba and Ce sites, $\sum Pr_{species} = Pr'_{Ce} + Pr^{x}_{Ce} + Pr^{\bullet}_{Ba} = x$

$$Ba_{\frac{1}{1+\alpha}}Pr_{\frac{\alpha}{1+\alpha}}Ce_{\frac{1-x}{1+\alpha}}Pr_{\frac{x-\alpha}{1+\alpha}}V''''_{Ce_{\frac{y}{1+\alpha}}}O_{3-\delta}, \qquad \text{(Model III)}$$

where $y \simeq 2\alpha$ and α is the number $Pr^{\bullet}_{Ba}$ which is fitted by the Rietveld method.

The results of applying the different structural models are discussed below. The detailed results with the goodness of fit for all the fits in the different models have been included in the supporting information.

Electrochemical impedance spectroscopy (EIS) was used to characterize the electrical behavior at 373 K in wet synthetic air, in order to compare the effect of Pr doping and to correlate structural parameters with transport properties.

3. Results and discussion

3.1. Study of Pr location

As was mentioned above, the XRD patterns indicate that all samples are single phase, displaying orthorhombic *Pnma* space-group symmetry (Knight, 2001). The systematic shift of Bragg peaks shows a reduction of the lattice parameters as Pr content increases. From ionic radii considerations this reduction would suggest that Pr goes to the Ba sites since the ionic radii of Pr^{3+} 12-fold coordinated is lower than Ba^{2+} ($r^{XII}_{Pr^{3+}}$ = 1.32 Å and $r^{XII}_{Ba^{2+}}$ = 1.61 Å), while Pr^{3+} and Pr^{4+} in sixfold coordination ($r^{VI}_{Pr^{3+}}$ = 0.99 Å, $r^{VI}_{Pr^{4+}}$ = 0.85 Å) are larger or similar to Ce^{+4}($r^{VI}_{Ce^{4+}}$ = 0.87 Å; Shannon, 1976).

The AXRD technique was used to evaluate which of these substitutions is most probable. Fig. 3(*a*) compares the normalized intensities in Q-space [$Q = (4\pi/\lambda)\sin\theta$] collected at 10 000 and 5962 eV for $BaCe_{0.2}Pr_{0.8}O_{3-\delta}$. The peaks at ~ 2.37 Å^{-1} (121/112/310 triplet) and ~ 2.48 Å^{-1} (220/202 doublet) present the most significant differences between these two energies, attributed to the anomalous dispersion of Pr at the near-absorption edge. Also, the relative intensity for anomalous diffraction signal increases gradually with Pr content (see Fig. 3*b*) since the reduction of the scattering factor of Pr is more evident as Pr doping increases.

Fig. 4 compares the fit of the normal and anomalous XRD patterns between 2.32 and 2.52 Å^{-1} regions in the three proposed models for the $BaCe_{0.4}Pr_{0.6}O_{3-\delta}$ perovskite. Table 2 compares the goodness-of-fit indicators (R_p, R_{wp} and χ^2) for the different models and energies by the multipattern fit mode. Similar results have been obtained for all compositions (see the supporting information).

The possibility of Pr fully located at Ba sites can be disregarded based on the poor fitting agreements of Model I, and the fact that a high concentration of Ce vacancies should unstabilize the structure. Otherwise, Models II and III showed similar goodness of fits. The partial substitution of Ba^{2+} and Ce^{4+} by lanthanides was also reported for $BaCe_{0.85}M_{0.15}O_{3-\delta}$ (M = Nd, Gd, Yb) perovskites (Wu, 2005). Wu *et al.* (2005) proposed that 4.6% of Yb and 13.6% of Gd reside at the Ba site, decreasing the concentration of oxygen vacancies from the ideal value of 7.5 mol % to ~ 7% and ~ 5.6% for Yb and Gd, respectively. These compounds exhibit lower proton conductivity than compounds doped with smaller ionic radii,

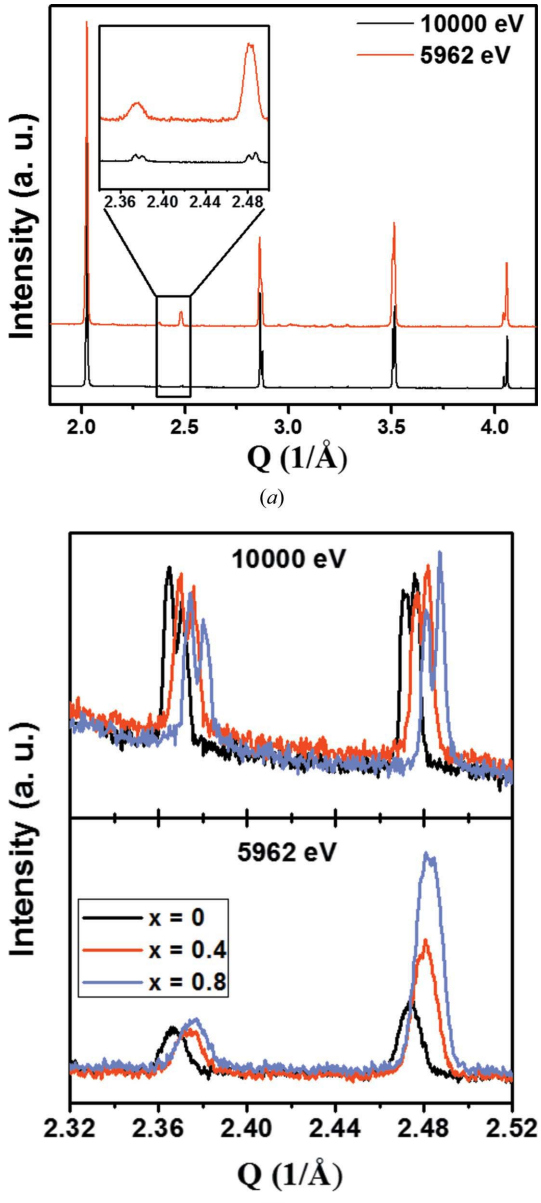

Figure 3
(*a*) Diffraction patterns collected at two different energies for the higher Pr content perovskite (x = 0.8). (*b*) Gradual change of relative intensity with Pr content for the diffraction patterns at two energies.

Table 3
Structural parameters of $x = 0.6$ for Model III, obtained from Rietveld fits. The goodness of fits for this composition are indicated in Table 2.

$x = 0.6$, space group *Pnma* (No. 62), $a = 6.19647$ (7), $b = 8.74999$ (9), $c = 6.22045$ (9) Å, $\alpha = \beta = \gamma = 90°$.

Atoms	Wyckoff position	Atomic positions			Occ.	Anisotropic vibrations × 10^2 (Å^2)		
		x	y	z		U^{11}	U^{22}	U^{33}
Ba	4*c*	0.0145 (1)	0.25	−0.0044 (1)	0.991 (1)	0.99 (1)	0.99 (1)	0.21 (1)
Pr1					0.009 (1)			
Ce	4*b*	0	0	0.5	0.396 (1)	0.32 (2)	0.48 (1)	0.26 (2)
Pr2					0.585 (1)			
O1	4*c*	−0.011 (1)	0.25	0.430 (1)	1	Isotropic vibration		
O2	8*d*	0.276 (1)	0.042 (1)	0.724 (1)	1	U_{iso} × 10^2 (Å^2)		
						0.29(6)		

Table 4
Lattice parameters of $BaCe_{1-x}Pr_xO_{3-\delta}$ perovskites (*Pnma* No. 62 space group).

x	a (Å)	b (Å)	c (Å)
0	6.21664 (7)	8.77789 (9)	6.23629 (9)
0.2	6.21025 (7)	8.76826 (9)	6.22886 (9)
0.4	6.20345 (7)	8.75952 (9)	6.22537 (9)
0.6	6.19647 (7)	8.74999 (9)	6.22045 (9)
0.8	6.18949 (7)	8.74009 (9)	

such as $BaCe_{0.9}Y_{0.1}O_{3-\delta}$ and $BaCe_{0.9}Yb_{0.1}O_{3-\delta}$ upon exposure to humid atmospheres (Amsif *et al.*, 2011). Then taking into account these considerations and the good agreement obtained by using Model III, this was adopted to study the crystal structure of these compounds. Table 3 shows the lattice parameters, atomic occupancy and positions, and anisotropic displacement parameters resulting from Model III for $BaCe_{0.4}Pr_{0.6}O_{3-\delta}$. The data for all compositions are included in the supporting information.

Then, considering that Pr could partially substitute Ba and Ce sites (Model III), Fig. 5 shows the Pr occupancy at Ba sites. The Pr^{3+} occupancy at the Ba site increases with doping, but in the case of a highly doped compound ($x = 0.8$) this reaches only 1.9% of the total Pr content. This is an expected result since Pr is able to present multiple valences (Pr^{4+}/Pr^{3+}) and the Ce^{4+} substitution must be favored over Ba^{2+}. Otherwise, the percentage of Pr^{3+} (with respect to the Pr total) in the Ba site, despite its low values, increases from 0.5 to 1.9% with Pr content. This slight substitution of Ba ions by Pr could be one of the reasons for the decrease of lattice parameter with Pr content. In the next section the effect of Pr on the crystal structure is discussed.

3.2. Effect of Pr doping on $BaCeO_{3-\delta}$ structure

According to the above AXRD analysis, the Pr ions are mainly located at Ce sites with a low percentage at Ba sites. The XRD data analysis shows that Pr doping preserves the orthorhombic symmetry decreasing the lattice parameters as Pr content increases.

Table 4 summarizes the cell parameters of $BaCe_{1-x}Pr_xO_{3-\delta}$ ($x = 0$, 0.2, 0.4, 0.6 and 0.8) perovskites. According to the ionic radii criterion, the decrease in lattice parameters should be mainly associated with the Ba substitution by Pr^{3+} ions instead of the presence of mixed-valence Pr^{3+}/Pr^{4+} at Ce sites.

The existence of the mixed Pr^{3+}/Pr^{4+} ions introduces O-vacancy defects and electronic conductivity in the Pr-doped $BaCeO_3$ compounds (Sharova *et al.*, 2005; Wang & Qiu, 2008; Mukundan *et al.*, 2001) making the Pr-doped $BaCeO_3$ perovskite potential mixed H-ionic and electronic conductor. Electrochemical impedance spectra (EIS) collected for dense $BaCe_{1-x}Pr_xO_{3-\delta}$ samples are shown in Fig. 6. The impedance spectra show two arcs, corresponding to bulk and grain boundary transport. Table 5 resumes the conductivity values of each contribution. It can be seen that Pr increases both conductivity processes. However, the contribu-

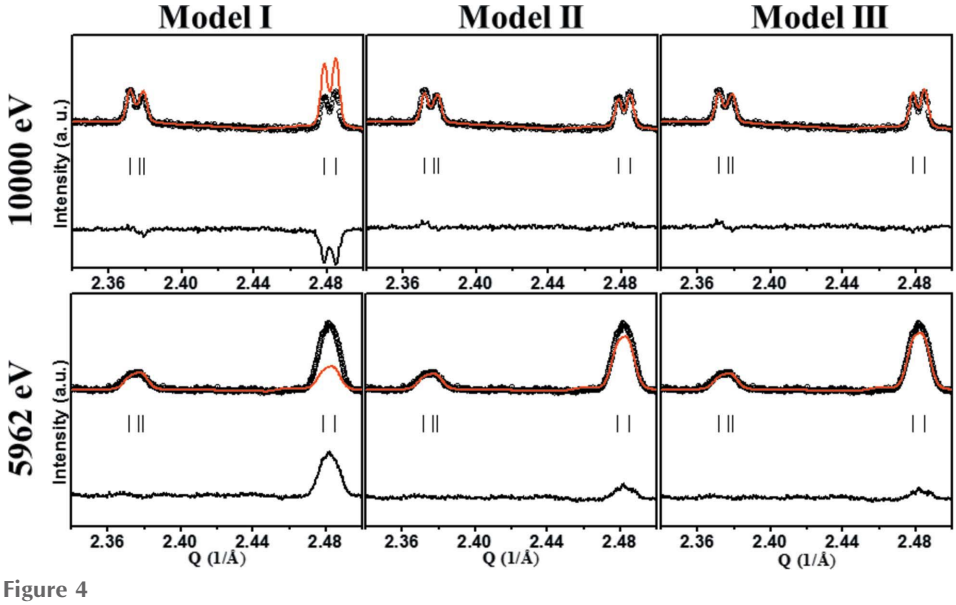

Figure 4
Experimental (circles), fitted (red lines) and the difference between both (black lines) diffraction patterns for $x = 0.6$ within the Q range of the major difference between normal (10 000 eV) and anomalous (5962 eV) diffraction. Models (I), (II) and (III) are explained in the text. Bragg positions are also indicated with short vertical bars.

Table 5
Conductivities values (μSm cm^{-1}) for $BaCe_{1-x}Pr_xO_{3-\delta}$ dense samples in wet synthetic air at 373 K.

x	Bulk	Grain boundary
0	0.00035	0.00011
0.2	0.12	0.37
0.4	5.32	8.58
0.6	1.78	0.53
0.8	115	1.64

tion of each process to the electronic conductivity is not resolved.

The electronic transport should occur through the (Ce/Pr)4*f*–O2*p* band and depends on the orbital overlap, whereas the proton conduction is usually described as a two-step Grotthuss-type diffusion mechanism, where the proton migration involves a quick 90° reorientation, followed by a transfer through the oxygen sites (Kreuer, 1999). DFT calculations on $BaCe_{1-x}Gd_xO_{3-\delta}$ perovskites (Hermet *et al.*, 2013) propose that in this highly distorted orthorhombic perovskite, and in contrast to the case of simple cubic perovskites such as $BaZrO_3$, the interoctahedral hopping is favored by octahedral tilting. This tilting shortens some of the O—O distances, favoring the hopping from one O-apical site towards the next one on the next near-neighbor octahedron. This is in agreement with that reported by Azad & Irvine (2009) from a neutron diffraction study on deuterated samples of $BaCe_{0.4}Zr_{0.4}Sc_{0.2}O_{2.90}$. This study suggests that the H^+ hopping in $BaCeO_3$ perovskites mainly involves the O1 interoctahedral sites through the shorter O1—O1 distance on the BaO planes.

Then, as the (Ce/Pr)—(Ce/Pr) distance is shortened and the (Ce/Pr)—O—(Ce/Pr) angle is close to 180°, the (Ce/Pr)4*f*–O2*p* orbital overlap increases and consequently the electronic conductivity. On the contrary, as the octahedral tilting decreases, and with this the difference between O1—O1 distances, the H interoctahedral hopping is reduced and also the H-conductivity. Otherwise, if the (Ba/Pr)—O1 distance decreases, the electrostatic repulsion between H ions and Ba increase and also the H^+ mobility. Furthermore, there is a compromise relationship between hopping distance and bond energy for H-migration as the octahedral distortion decreases.

Fig. 7 shows the (Ce/Pr)—(Ce/Pr) distances and the (Ce/Pr)—O—(Ce/Pr) angles, and Fig. 8 indicates (Ba/Pr)—O1 and O1—O1 as a function of Pr content. From Figs. 7 and 8 it can be seen that the Pr doping decreases long distances, and increases short ones for (Ba/Pr)—O1 and O1—O1, lowering octahedral tilt and the orthorhombic distortion. Also, the Pr doping decreases the short and long (Ce/Pr)—(Ce/Pr) distances and increases the (Ce/Pr)—O1—(Ce/Pr) and (Ce/Pr)—O2—(Ce/Pr) angles, improving the overlapping of (Ce/Pr)—O orbitals.

Therefore, the decrease in octahedral distortion enhances the overlap of the orbitals, which is in agreement with the

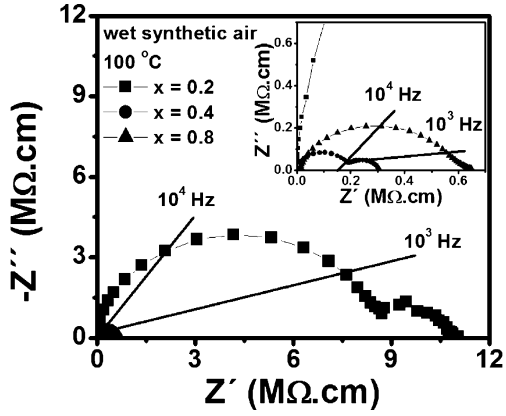

Figure 6
Impedance spectra for dense samples in wet synthetic air at 373 K. The frequencies are indicated.

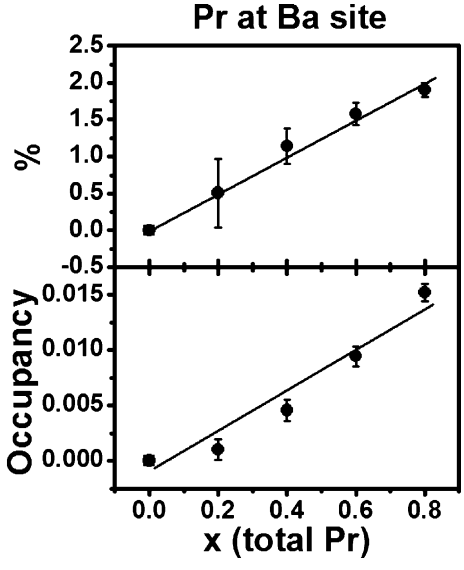

Figure 5
Pr occupancy and percentage at Ba sites as a function of Pr content.

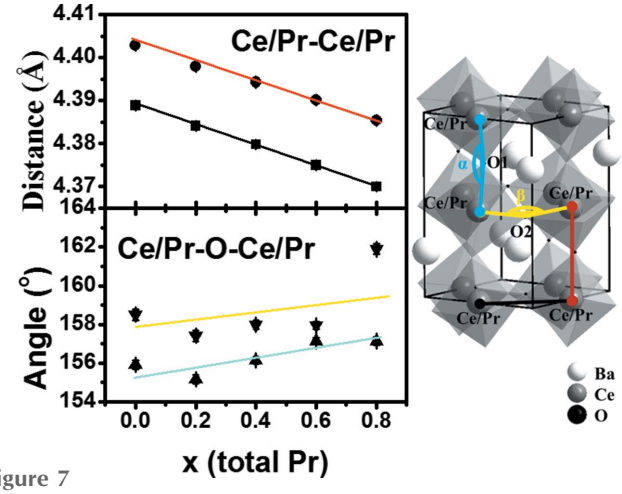

Figure 7
(Ce/Pr)—(Ce/Pr) short (squares) and long (circles) distances, and (Ce/Pr)—O1—(Ce/Pr) (triangles) and (Ce/Pr)—O2—(Ce/Pr) angles (inverted triangles) (α and β, respectively), from Model III, as a function of Pr content. The distances and angles are indicated on the structure.

increase in electrical conductivity previously reported (Basbus *et al.*, 2014; Sharova *et al.*, 2005; Wang & Qiu, 2008; Mukundan *et al.*, 2001). Besides, the decrease in orthorhombic distortion could produce a reduction of the protonic mobility, despite the fact that the Pr^{+3} substitution increases the oxygen vacancy concentration and therefore the H_2O incorporation.

4. Conclusion

By a combination of structural refinements of the XRD data collected near and far from the Pr L_{III} absorption edge it can be concluded that Pr is mainly located in the Ce site. A small concentration of Pr is located at the Ba sites and increases as the total Pr content increases too, but to a lesser degree than that observed in other lanthanides. This effect is probably due to the fact that the mixed valence Pr^{3+}/Pr^{4+} promotes the Ce^{4+} substitution over that of Ba^{2+}.

As a consequence of Pr doping, not only the mixed Pr^{3+}/Pr^{4+} states can contribute to the electronic conductivity but also the orthorhombic distortion decreases, thus promoting electronic conduction. The Pr doping produces two opposite effects on the H-ionic conductivity. The Pr doping reduces the orthorhombic distortion decreasing the proton mobility due to a larger hopping distance, whereas this doping increases the oxygen vacancy concentration and therefore the H_2O incorporation.

APPENDIX *A*

Different lattice defects are produced as a consequence of Pr substitution. The defect structure is the result of the different site location, the electroneutrality condition and site balances.

$$[Pr^{\bullet}_{Ba}] + 2[V^{\bullet\bullet}_{O}] = [Pr'_{Ce}] + 4[V''''_{Ce}] \quad (4)$$

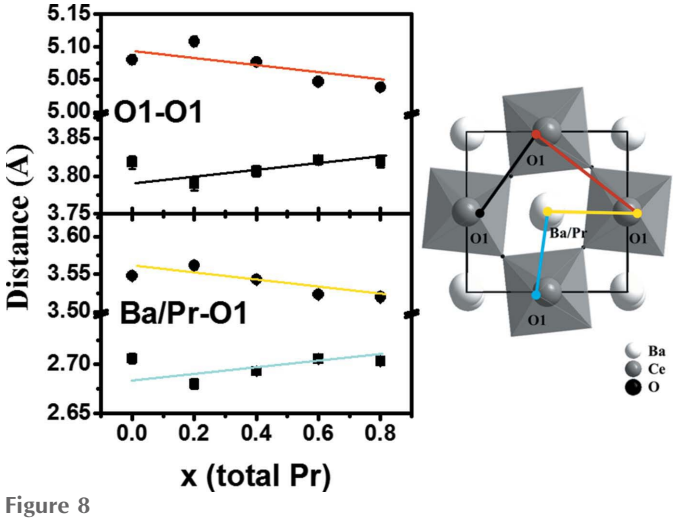

Figure 8
(Ba/Pr)—O1 and O1—O1 [short (squares) and long (circles)] distances from fitting with Model III as a function of Pr content. The distances are indicated on the projection of the *ac* plane.

$$[Pr^{\bullet}_{Ba}] + [Ba^{x}_{Ba}] = 1 \quad (5)$$

$$[Pr'_{Ce}] + [Pr^{x}_{Ce}] + [Ce^{x}_{Ce}] + [V''''_{Ce}] = 1 \quad (6)$$

$$[V^{\bullet\bullet}_{O}] + [O^{x}_{O}] = 3 \quad (7)$$

The species concentrations are expressed as partial molar fractions. Then for the $BaCe_{1-x}Pr_xO_{3-\delta}$ composition, the concentrations should be re-normalized as

$$[Ba^{x}_{Ba}] = \frac{1}{\text{species on Ba sites}} \quad (8)$$

$$[Ce^{x}_{Ce}] = \frac{1-x}{\text{species on Ce sites}}, \quad (9)$$

where x is the number of Pr atoms by unit formula, which means that

$$\sum Pr_{\text{species}} = Pr'_{Ce} + Pr^{x}_{Ce} + Pr^{\bullet}_{Ba} = x \quad (10)$$

The existence of a low amount of oxygen vacancies is needed to assure the electroneutrality of the oxide. However, it was assumed that $[V^{\bullet\bullet}_{O}] = \delta \simeq 0$ during the refinements as a consequence of the low sensibility of X-rays to detect O in the presence of heavy metal. Considering these equations, three different models were tested:

Model I: Pr fully located at the Ba site, which means that equation (10) is reduced to $\sum Pr_{\text{species}} = Pr^{\bullet}_{Ba} = x$.

Therefore, considering that the species on Ba sites are $1 + x$, the partial molar fraction n of Pr in Ba sites is

$$[Pr^{\bullet}_{Ba}] = \frac{x}{1+x}$$

and the site balance in equation (5) can be rewritten as

$$[Ba^{x}_{Ba}] + [Pr^{\bullet}_{Ba}] = 1 = \frac{1}{1+x} + \frac{x}{1+x}.$$

On the other hand, the species on Ce sites are $1 - x + y$, where y is the minimum number of cerium vacancies V''''_{Ce} produced to compensate the charge of the $Pr^{\bullet}_{Ba}$. Then, the site balances in equation (6) is given by

$$[Ce^{x}_{Ce}] + [V''''_{Ce}] = 1 = \frac{1-x}{1-x+y} + \frac{y}{1-x+y}.$$

The minimum amount of V''''_{Ce} produced (y) can be estimated from the charge balance in equation (4) by assuming $[V^{\bullet\bullet}_{O}] = 0$

$$[Pr^{\bullet}_{Ba}] = 4[V''''_{Ce}] = \frac{x}{1+x} = 4\frac{y}{1-x+y}$$

then $y = [x(1-x)]/(4+3x)$.

The oxide composition can be rewritten as $Ba_{1/(1+x)}Pr_{x/(1+x)}Ce_{(1-x)/(1-x+y)}V_{Ce''''_{y/(1-x+y)}}O_{3-\delta}$.

Model II: Pr fully located at the Ce site. In this case, the species on Ba sites are 1 and the species on Ce sites = 1, while equation (10) is reduced to $\sum Pr_{\text{species}} = Pr'_{Ce} + Pr^{x}_{Ce} = x$ and the oxide composition is $BaCe_{1-x}Pr_xO_{3-\delta}$.

Model III: Pr free distributed between Ba and Ce sites.

In this case, it is impossible to discriminate in advance the number of Pr^{3+} and Pr^{4+} located in Ce sites. However, it is possible to define an α parameter as the number of Pr located

on Ba sites. Then, equation (10) is split as $Pr^{\bullet}_{Ba} = \alpha$ and $Pr'_{Ce} + Pr^{x}_{Ce} = x - \alpha$. In this model α is a parameter to be fitted from Rietveld refinement.

Then, the species on Ba sites are $1 + \alpha$, and the site balance in equation (5) gives

$$[Ba^{x}_{Ba}] + [Pr^{\bullet}_{Ba}] = 1 = \frac{1}{1+\alpha} + \frac{\alpha}{1+\alpha}.$$

On the other hand, the species on Ce sites are $(1 - x) + (x - \alpha) + y$, where y is also referred to the number of produced cerium vacancies V''''_{Ce} produced. Then, the site balance in equation (6) is

$$[Ce^{x}_{Ce}] + \left([Pr'_{Ce}] + [Pr^{x}_{Ce}]\right) + [V''''_{Ce}] = 1 = \frac{1-x}{1-\alpha+y} + \frac{x-\alpha}{1-\alpha+y} + \frac{y}{1-\alpha+y}.$$

In this case, it is impossible to apply the charge balance in equation (4) to estimate the number of cerium vacancies V''''_{Ce} due to the fact that Pr'_{Ce} also compensates the $Pr^{\bullet}_{Ba}$ and this fraction is still undetermined. However, the α parameter is a measurement of the partial distribution of Pr between both the Ba and Ce sites, and therefore the total number of species in each site should be the same

$$\text{species in Ba sites} = 1 + \alpha = \text{species in Ce sites} = (1 - x) + (x - \alpha) + y$$

and then $y = 2\alpha$ and the oxide composition is $Ba_{1/(1+\alpha)}Pr_{\alpha/(1+\alpha)}Ce_{(1-x)/(1+\alpha)}Pr_{(x-\alpha)/(1+\alpha)}V''''_{Ce_{y/(1+\alpha)}}O_{3-\delta}$.

Note that the limit situations of Model III where $Pr^{\bullet}_{Ba} = \alpha = 0$ recover Model II, whereas $Pr^{\bullet}_{Ba} = \alpha = x$ must recover Model I. However, in this last case V''''_{Ce} is the maximum ($y = 2x$) produced as a consequence of the site balance. Thus, for Model I $x/[4(1 + x)] < [V''''_{Ce}] < 2x/(1 + x)$, where the minimum is needed to assure the electroneutrality (assuming $[V^{\bullet\bullet}_{O}] = \delta \simeq 0$). The Rietveld fit was performed with the minimum condition V''''_{Ce}.

Acknowledgements

This work was supported by CNEA (Argentinean National Commission of Atomic Energy), CONICET (Argentinean National Council of Scientific and Technical Research), UNCu (National University of Cuyo), ANPCyT (National Agency for Science and TechnologyPromotion) and LNLS (Brazilian National Laboratory of Synchrotron Radiation, Campinas, Brazil).

References

Amsif, M., Marrero-López, D., Ruiz-Morales, J. C., Savvin, S. N. & Núñez, P. (2011). *J. Power Sources*, **196**, 9154–9163.
Azad, A. K. & Irvine, J. T. S. (2009). *Chem. Mater.* **21**, 215–222.
Basbus, J. F., Moreno, M., Caneiro, A. & Mogni, L. V. (2014). *J. Electrochem. Soc.* **161**, F969–F976.
Bi, L., Zhang, S., Zhang, L., Tao, Z., Wang, H. & Liu, W. (2009). *Int. J. Hydrogen Energy*, **34**, 2421.
Bonanos, N. (2001). *Solid State Ionics*, **145**, 265–274.
Caticha-Ellis, S. (1981). *Anomalous Dispersion of X-rays in Crystallography.* University College Cardiff Press.
Connor, S. T., Weil, B. D., Misra, S., Cui, Y. & Toney, M. F. (2013). *Chem. Mater.* **25**, 320–325.
Cullity, B. D. & Stock, S. R. (1978). *Elements of X-ray Diffraction*, 2nd ed. New York: Addison–Wesley.
Ferreira, F. F., Granado, E., Carvalho Jr, W., Kycia, S. W., Bruno, D. & Droppa Jr, R. (2006). *J. Synchrotron Rad.* **13**, 46–53.
Finger, L. W., Cox, D. E. & Jephcoat, A. P. (1994). *J. Appl. Cryst.* **27**, 892–900.
Giannici, F., Longo, A., Kreuer, K.-D., Balerna, A. & Martorana, A. (2010). *Solid State Ionics*, **181**, 122–125.
Giannici, F., Shirpour, M., Longo, A., Martorana, A., Merkle, R. & Maier, J. (2011). *Chem. Mater.* **23**, 2994–3002.
Gill, S., Kannan, R., Maffei, N. & Thangadurai, V. (2013). *RSC Adv.* **3**, 3599–3605.
Glöckner, R., Islam, M. S. & Norby, T. (1999). *Solid State Ionics*, **122**, 145–156.
Hermet, J., Torrent, M., Bottin, F., Dezanneau, G. & Geneste, G. (2013). *Phys. Rev. B*, **87**, 104303.
Hodeau, J.-L., Favre-Nicolin, V., Bos, S., Renevier, H., Lorenzo, E. & Berar, J.-F. (2001). *Chem. Rev.* **101**, 1843–1867.
Iwahara, H., Uchida, H. & Morimoto, K. (1990). *J. Electrochem. Soc.* **137**, 462–465.
Iwahara, H., Uchida, H., Ono, K. & Ogaki, K. (1988). *J. Electrochem. Soc.* **135**, 529–533.
Kikuchi, J., Koga, S., Kishi, K., Saito, M. & Kuwano, J. (2008). *Solid State Ionics*, **179**, 1413–1416.
Knight, K. (2001). *Solid State Ionics*, **145**, 275–294.
Knight, K. & Bonanos, N. (1995). *Mater. Res. Bull.* **30**, 347–356.
Kreuer, K.-D. (1999). *Solid State Ionics*, **125**, 285–302.
Kreuer, K. D. (2003). *Annu. Rev. Mater. Res.* **33**, 333–359.
Liu, J. F. & Nowick, A. S. (1992). *Solid State Ionics*, **50**, 131–138.
Magrasó, A., Frontera, C., Gunnaes, A., Tarancón, A., Marrero-López, D., Norby, T. & Haugsrud, R. (2011). *J. Power Sources*, **196**, 9141–9147.
Magrasó, A., Kjølseth, C., Haugsrud, R. & Norby, T. (2012). *Int. J. Hydrogen Energy*, **37**, 7962–7969.
Medvedev, D., Murashkina, A., Pikalova, E., Demin, A., Podias, A. & Tsiakaras, P. (2014). *Prog. Mater. Sci.* **60**, 72–129.
Mukundan, R., Davies, P. K. & Worrell, W. L. (2001). *J. Electrochem. Soc.* **148**, A82–A86.
Norby, T. (1999). *Solid State Ionics*, **125**, 1–11.
Palancher, H., Bos, S., Bérar, J. F., Margiolaki, I. & Hodeau, J. L. (2012). *Eur. Phys. J.* **208**, 275–289.
Paudel, T. R., Lany, S., d'Avezac, M., Zunger, A., Perry, N. H., Nagaraja, A. R., Mason, T. O., Bettinger, J. S., Shi, Y. & Toney, M. F. (2011). *Phys. Rev. B*, **84**, 064109.
Pelletier, L., McFarlan, A. & Maffei, N. (2005). *J. Power Sources*, **145**, 262–265.
Perkins, J., Paudel, T. R., Zakutayev, A., Ndione, P., Parilla, P., Young, D., Lany, S., Ginley, D., Zunger, A., Perry, N. H., Tang, Y., Grayson, M., Mason, T. O., Bettinger, J. S., Shi, Y. & Toney, M. F. (2011). *Phys. Rev. B*, **84**, 205207.
Shannon, R. D. (1976). *Acta Cryst.* A**32**, 751–767.
Sharova, N. V., Gorelov, V. P. & Balakireva, V. B. (2005). *Russ. J. Electrochem.* **41**, 665–670.
Wang, M.-Y. & Qiu, L.-G. (2008). *Chin. J. Chem. Phys.* **21**, 286–290.
Welzmiller, S., Urban, P., Fahrnbauer, F., Erra, L. & Oeckler, O. (2013). *J. Appl. Cryst.* **46**, 769–778.
Wu, J. (2005). PhD Thesis, California Institute of Technology.
Wu, J., Webb, S. M., Brennan, S. & Haile, S. M. (2005). *J. Appl. Phys.* **97**, 054101.
Yang, R., Bian, W., Strasser, P. & Toney, M. F. (2013). *J. Power Sources*, **222**, 169–176.
Yang, R., Leisch, J., Strasser, P. & Toney, M. F. (2010). *Chem. Mater.* **22**, 4712–4720.
Zuo, C., Zha, S., Liu, M., Hatano, M. & Uchiyama, M. (2006). *Adv. Mater.* **18**, 3318–3320.